Journal of Solid Mechanics Vol. 11, No. 4 (2019) pp. 736-746
DOI: 10.22034/jsm.2019.668764

Investigating the Effect of Joint Geometry of the Gas Tungsten Arc Welding Process on the Residual Stress and Distortion using the Finite Element Method

A. Shiri, A. Heidari *

Department of Mechanical Engineering, Khomeinishahr Branch, Islamic Azad University, Khomeinishahr, Isfahan, Iran

Received 8 July 2019; accepted 10 September 2019

ABSTRACT

Although a few models have been proposed for 3D simulation of different welding processes, 2D models are still more effective in design goals, thus more popular due to the short-time analysis. In this research, replacing "time" by the "third dimension of place", the gas tungsten arc welding process was simulated by the finite element method in two dimensions and in a short time with acceptable accuracy in two steps (non-coupled thermal and mechanical analysis). A new method was proposed for applying initial conditions using temperature values calculated in the preceding step of the solution; this trick reduces nonlinear effects of birth of elements and considerably reduces analysis time. A new parameter was defined for determining thermal boundary conditions to determine the contribution of the imposed surface and volumetric thermal loads. The effect of weld joint geometry on residual stresses and distortion was studied based on a validated simulation program. Results suggest that changing the joint geometry from *V*-into *X*-groove, the maximum values of residual stress and distortion are reduced by 20% and 15%, respectively.

Keywords: Gas tungsten arc welding; Joint geometry; Residual stress; Distortion; Finite element method.

1 INTRODUCTION

FUSION welding is extensively used as a joint method in different industries such as metal structures, tubing, and automotive industries [1]. The major factors causing residual stresses and strains in these parts include the plastic strain created in the body due to the steep temperature gradient and the strains caused by phase transformations during a thermal cycle [2]. The residual stress around a weld reduces structural integrity. On the other hand, the high tensile residual stress near a weld zone causes embrittlement, reduces structure lifetime, and leads to stress corrosion during service Distortion has a negative impact on the appearance of welded joints and reduces the accuracy and correctness of joints assembly [3-5]. Therefore, predicting structure conditions after

*Corresponding author. Tel.: +98 31 33660012; Fax: +98 31 33660088.
E-mail address: heidari@iaukhsh.ac.ir (A. Heidari).

welding such as residual stresses and distortion is very important for designers. In the past, welding residual stresses were calculated by experimental measuring methods, which were often costly and time-consuming. Therefore, researchers attempted to determine residual stresses and distortion over the last few decades using analytical methods such as the finite element method. Cho and Kim [6] presented a new model for the consideration of phase transformations in a fusion welding process and achieved the residual stresses caused by gas tungsten arc welding (GTAW). They proved that the effect of consideration of phase transformations on residual stresses is significant in medium- and high-carbon steel; however, the effect is highly negligible in low-carbon steel. Chang and Teng [7] studied thermal elastic-plastic analysis using the finite element method for analyzing the thermomechanical behavior and estimation of residual stresses in welded butt joints. They also measured surface residual stresses using the *X*-ray diffraction method and compared them with the simulation results. They used the ability of the element birth and death for modeling a three-pass GTAW. Yajiang et al. [8] studied residual stress distribution in the weld joint of high-strength steel plates in ANSYS. The results indicated a severe stress gradient around weld zone and specified that stress normal to the welding direction have a greater impact on crack formation as compared to stresses along the other directions. Vasudevan [9] studied a weld bulge created by A-TIG method on 316LN and 304LN austenite stainless steels and discovered the essential role of geometry in determining the mechanical properties and weld quality. Palanichamy et al. [10] measured the surface and subsurface residual stresses in austenite stainless steel weld joints using an ultrasonic technique. The technique is based on the effect of stresses on the velocity of development of elastic waves. Tseng and Hsu [11] showed that welding using GTAW process with a type of activating flux has the maximum penetration on the base metal of austenite stainless steels and the minimum distortion. Ganesh et al. [12] performed the thermal-mechanical analysis of GTAW on 316LN austenite stainless steels. They employed two non-destructive testing methods (*X*-ray and ultrasonic testing) for verifying stress distribution, used Infrared Thermography for temperature distribution, and a digital altimeter for distortion. Bhatti et al. [13] studied the impact of thermal-mechanical properties in different steel groups on residual stress and distortion of *T*-groove joints using ANSYS. They concluded that it was possible to consider all thermal-mechanical properties fixed except yield strength to evaluate residual stress. They also discovered that thermal capacity parameter, yield strength, and thermal expansion coefficient should be considered temperature-dependent to examine distortion. Vasantharaja et al. [14] studied experimentally the effect of TIG and A-TIG welding processes on the microstructure, residual stresses and distortion with different joint configurations. In order to minimize residual stresses and distortion, the double side is recommended for the weld joint. Varma Prasad et al. [15] simulated a TIG weld in the circumferential joints of stainless steel pipes using coding in ANSYS. They studied the impact of current and pipe thickness on temperature and residual stress distribution. Bajpei et al. [16] studied the GMAW process of thin aluminium alloy sheets using different heat sink models to reduce residual stresses and distortion. They concluded that the heat sink model using a mixture of argon gas and water is the most appropriate plan to achieve the minimum residual stress and distortion. Zubairuddin et al. [2] simulated a GTA multi-pass welding process for Grade 91 steel. Their simulation and experimental results revealed that heating a sheet during welding passes up to $200°C$ might reduce distortion.

In this study, the gas-shielded tungsten arc welding (GTAW) process, also known as the tungsten inert gas (TIG) welding, has been simulated by replacing "time" by the "third dimension of place" using the finite element method. Two features are considered in this macro programs to use them in design objectives: the analysis should be accurate and performed in the shortest time; and the program should be fully parametric. The welding process simulation is performed in two steps of nonlinear non-coupled thermal and mechanical solution. Thermal history and stresses distribution are obtained from the thermal solution and mechanical solution, respectively. A comparison was made among the results of the simulation program, the research experimental results, and the results presented by other researchers. Finally, the effects of weld joint geometry on residual stresses and distortion was studied.

2 THE FINITE ELEMENT MODEL

This research considered the joint of two similar $110\times30\times4.5mm$ plates with *V* and *X*-groove joint plans. Weld seam gap is 2 *mm*. Fig.1 shows the model geometry and coordinate system. The model is examined in 2D with plane-strain behavior. With respect to the symmetry, only half of the model is simulated.

Fig.2 shows model meshing method. Due to the severe gradient of temperature and stress around the weld zone, this zone is more important. Therefore, a finer meshing is used in this zone.

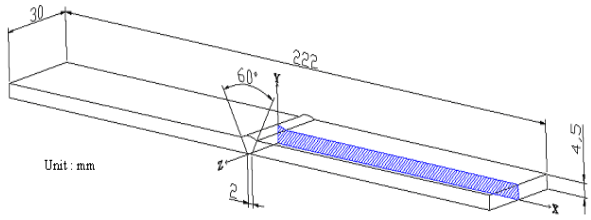

Fig.1
Model geometry and coordinate system.

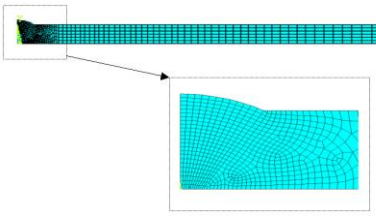

Fig.2
Model meshing.

As it is not possible to generate or remove elements during solution time, all the elements should be generated from the beginning. Therefore, the ability of birth and death of elements is used for modelling a multi-pass weld. This method uses the death of elements instead of removing them. For the death of elements, a reducing coefficient is multiplied by the stiffness of the elements. Although the force vector of the dead element is zero it appears in the force vector of elements, and also mass, specific heat, and other effects tend to zero. Therefore, the mass and energy of the dead elements are not calculated in the sum of mass and total energy of the model. Similarly, the ability of birth of elements is used in this method instead of adding an element to the model. For the birth of elements, stiffness coefficient, mass, element force, etc. return to their initial values [3, 17].

The welding method in this article is GTA welding process. Table 1, specifies the welding parameters. Fig. 3 shows the order of passes in the *V*- and *X*-groove joint plans. The interval between passes is 330 seconds and the solution is continued after the third pass as soon as the structure temperature reaches the ambient temperature.

Table 1
Welding parameters for each pass [7].

Pass	Current (A)	Voltage (V)	welding speed (mm/s)
1	85	25	1
2	85	26	0.75
3	85	25	0.55

(a) V-groove joint (b) X-groove joint

Fig.3
Order of welding passes.

Three levels were defined in the present simulation program for problem parameters: Level 1 encompasses the geometrical parameters of work piece and machine set points such as the length, width, thickness, wire diameter, welding speed, voltage, and amperage. These parameters can be accessed very easily. When the program starts, default values are shown in some windows and the windows are used to change the parameters. The parameters of Level 2 include the material thermos-physical specifications that should be changed by changing material. These parameters, which are mainly temperature-dependent, were stored in the sub-files of the program. Level 3 includes the settings of the finite element model such as quantity and density of mesh, type of solver, and similar items whose edition are only possible through changing the program. With change in the parameters of the Level 3, the program must be validated again.

3 MATERIAL SPECIFICATIONS

ASTM A36 steel has a ferrite-pearlite structure and is extensively used for various constructions. It offers excellent weld ability and never exhibits specific thermal behaviour during welding. Table 2., shows the concentration (*wt*%) of constituent elements.

Table 2
Chemical Compositions (%) of ASTM A36 steel.

C	Mn	P	S	Si	Ni	Cr	Mo	Cu	Fe
0.16	0.69	0.033	0.039	0.21	<0.10	<0.08	<0.10	<0.10	Bal.

As Fig. 4 shows, the mechanical and thermos-physical properties of the steel are a function of temperature. This figure represents that with increasing temperature, the Young's modulus, yield strength, and thermal conductivity coefficient reduce, while the thermal expansion coefficient and specific heat coefficient increase. It is assumed in the simulation that base metal, the heat affected zone, and weld metal properties are identical [7, 18, 19]. It is assumed that the material follows Von Mises yield criterion and flow rule. Work-hardening rule is considered as linear isotropic hardening. Phase transformations are overlooked due to the low carbon content in the base steel [6, 20, 21].

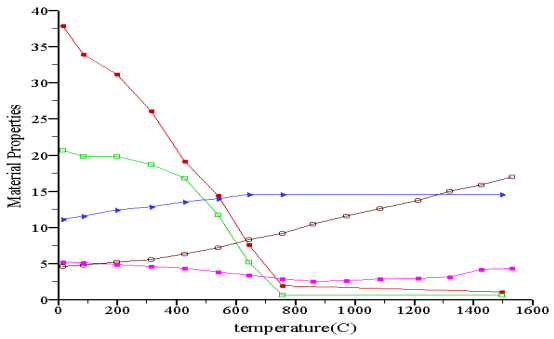

Material property	Symbol	Dimension
Yield strength	● --- σ_y	$10^7 Pa$
Young's modulus	□ --- E	$10^{10} Pa$
Thermal expansion coefficient	▲ --- α	$\mu m / m^\circ C$
Thermal conductivity	■ --- k	$10\, W / m^\circ C$
Specific heat	○ ---c	$10^2 J / Kg^\circ C$

Fig.4
Temperature-dependent thermal physics and mechanical properties of ASTM A36 [7].

4 THERMAL MODEL

The effect of thermal flux along the weld line can be neglected where welding speed is much higher than thermal diffusion along this line ($\partial T / \partial z = 0$) [6]. Therefore, the 2D model assumption will hold. Considering time limitations in the industry and the fact that the speed of the 2D solution is higher than the one of the 3D solution, this research simulates the 2D model with a plane-strain behaviour. Assuming this, the thermal flux is limited to the cross-section perpendicular to weld direction in x-y coordinate. As the heat of plastic strain, the effect of stresses on phase transformations, and changes of the coefficient of convection heat transfer caused by surface strains are negligible, it is possible to solve mechanical and thermal equations independently and use a non-coupled solution in welding [7, 8]. Due to symmetry, convection heat transfer coefficient in the central line was considered zero and it was considered $15\, W / m^2 k$ for the remaining surfaces. Ambient temperature was considered $18^\circ C$. To consider the impact of weld pool fluid current, heat conduction is raised by a coefficient for the temperature higher than the melting point. The effect of the latent heat of phase change is considered by the increase of specific heat coefficient at the temperature of phase change [6, 22, 23].

The Plane77 element that is a 2-D, 8-node thermal element was used in the thermal model. The proposed method uses the temperature values calculated in the preceding step as initial conditions; this trick reduces the nonlinear effects of the birth of elements and computation time.

5 THERMAL LOADING

Different methods have been proposed by researchers for applying the heat from an electric arc. Some of the major methods are as follows [16, 24-27]:

1. Applying very high initial temperature to the melting zone.
2. Applying a predetermined thermal cycle to the melting zone in a specific period of time.
3. Assuming a volumetric heat source in the melting zone in a specific period of time.
4. Applying a surface heat flux to the melting zone in a specific period of time.
5. A combination of the above methods.

In the fifth method, which is typically considered the most thorough of them all, the contribution of each of the above methods to the thermal power can be determined based on the physical events during a process. Generally, the joint formed by welding consists of the following steps:

I. The droplet/droplets enter the weld zone from an electrode and form the weld zone together with some of the molten metal that entered this zone. The contribution of each part to the formation of the weld zone can be calculated based on dilution, which depends on welding type and conditions. This phenomenon can be simulated as the birth of weld zone elements at an initial temperature of T_o, that can be calculated based on dilution (D):

$$T_o = \left[(1-D) T_{el}^{in} + D\ T_{ed} \right] \tag{1}$$

where T_{el}^{in} is the temperature of the droplet entering the weld pool from an electrode. Obviously, the droplet temperature is higher than the melting temperature of electrode material $\left(T_{el}^{m}\right)$ and lower than its boiling point $\left(T_{el}^{e}\right)$:

$$T_{el}^{m} \le T_{el}^{in} \le T_{el}^{e} \tag{2}$$

T_{ed} is the average temperature of the wall of weld zone when the droplet enters into the weld pool. It is easy to calculate to what depth the averaging is carried out; this is performed based on conservation of mass and knowing the dilution, mass flow rate of electrode droplets, pool dimensions, and welding speed. This method has a fundamental assumption, which is consideration of a fixed depth for the melted zone of a work piece. The trial and error method should be used for calculating Eq. (1), as T_{ed} is unknown. Therefore, the initial T_o is guessed first and then the Eq. (1) is checked after solving the problem. However, it should be considered that the share of weld energy transferred to the work piece in this method is negligible and the range of T_o between the melting temperature $\left(T_{wp}^{m}\right)$ and the pool metal evaporation $\left(T_{wp}^{e}\right)$ is variable:

$$T_{wp}^{m} \le T_o \le T_{wp}^{e} \tag{3}$$

The range for low-carbon steels is between 1400 to 3000 °*C*. As the 2D model is as large as the unit thickness, the volume of the bevelled area is $1 \times A$ in which A is the surface filled with molten material in each pass. For a desired welding speed of v, H_I is the share of welding energy transferred to a sheet through the initial condition of birth of elements at T_o temperature in the bevelled area, which is assumed the same pool.

$$H_I = \int_{T_i}^{T_o} vA\,\rho C dT \tag{4}$$

In the above equation, ρ is the density and *C* is the specific heat of the metal, which may vary with temperature. T_i is the initial temperature of the work piece, which is assumed equal to the ambient temperature. If the heat of phase transformations is considerable, its effect can be equalized in *C*. Given the fact that the element birth process is momentary, and the solution encounters many convergence problems at the corresponding moment, on the other hand the contribution of H_I to the total energy transferred is negligible, it was proposed to perform the first weld

pass at ambient temperature and to perform the ensuing passes at the temperature calculated for dead elements at birth time. This approximation considerably reduces the solution time.

II. When the weld zone is formed, it is exposed to a considerable heat flux during the time the electrode is on its surface due to electric arc radiation. In most 3D analyses, a Gaussian flux distribution on an object surface is proposed whose range is a zone with the diameter of two to three times bigger than the one of electrode diameter. The zone crosses the object surface at the velocity v .

In the 2D solution in which one cross-section of an object is considered, the distribution is applied as a function of time to the object surface. It is the time to replace the third dimension of the problem using this idea. This is a transient and 2D problem from the perspective of an observer on the welding electrode. It is clear that the heat affects the surface of the weld zone by radiation (radiation from the arc to the pool surface) and conduction (contact between the hot gas with the pool surface).

Considering that the weld pool is molten, heat flow penetrates to its depth from surface conductively and convectively. Determination of the share of each heat transfer method depends on weld geometry, amount and operation of buoyancy forces, magnetic forces, melt properties, and other factors. The higher the turbulence in a weld pool is, the higher the share of convective heat transfer will be. As mass transfer analysis is not simulated, this effect is replaced by a heat source. Figure 5 shows how to replace the effect of turbulence in the pool, which makes melt transfer heat from surface to the depth of the pool, by a heat source.

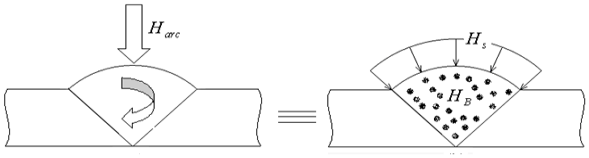

Fig.5
Equivalence of electric arc radiation and turbulence in pool by surface and volumetric heat sources.

If φ indicates the contribution of each of the above methods (surface flux power H_S and volumetric flux power H_B) to heat transfer to the pool, as:

$$H_{total} = \eta VI = H_I + H_{arc} \tag{5}$$

$$H_{arc} = H_S + H_B \tag{6}$$

$$H_S = \varphi H_{arc} \tag{7}$$

$$H_B = (1-\varphi) H_{arc} \tag{8}$$

where η is welding efficiency. Although η is associated with a wide range, most references recommended the range of 0.2 – 0.4 for GTA welding [12, 16, 25]. This research considers $\eta = 0.22$. To calculate surface loading intensity (q) and volumetric loading intensity (B) for a 2D model with unit thickness, we can write the equations like these:

$$q = \frac{H_S}{(md)^2} \tag{9}$$

$$B = \frac{H_B}{(md).A} \tag{10}$$

where d is the electrode diameter and m is the apparent coefficient for electrode diameter increase. When the distance of an electrode to the surface of a work piece increases, as Gaussian flux distribution is applied in a thicker circle in a more diffusing manner, the coefficient of m increases. This coefficient can even be considered lower than one.

The above equations describe the initial conditions and boundary conditions of the thermal transient problem. Due to the very high melting point of the tungsten electrode and very low rate of the melting electrode, dilution (D) was considered 100% in the GTA welding. When comparing H_1 with other similar terms in practical examples, the initial energy share of weld pool will be smaller than 5%. The recommendation made in Section (I), i.e. the use of the calculated temperature when there is a dead element in the model, makes this share zero in the first pass and reduces it about 2% in the following passes. This can be overlooked when compared with the advantage it provides in increasing solution velocity. On the other hand, the structure of Eq. (5) is in a way that the share of energy related to other sections has been added and it is compensated in terms of quantity (not in form of energy transfer). Also this research considers $\varphi = 0$ and uses the Goldak's double ellipsoidal heat source model for applying volumetric loading (Fig. 6).

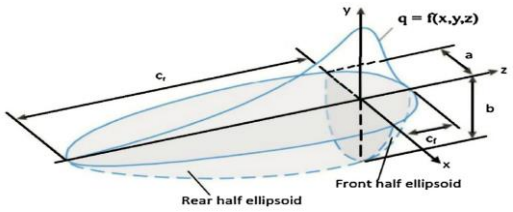

Fig.6
Goldak's double ellipsoidal power density heat source [25].

6 MECHANICAL MODEL

Thermal and mechanical solutions are performed successively. The thermal solution specifies temperature distribution during the welding process and then the thermal history is applied to the mechanical model as a thermal load and the stress distribution and distortion are achieved from the mechanical solution. Except for the type of element and boundary conditions used in the mechanical model, other items are similar to the thermal model. In the mechanical model, Plane82 element, which is a 2-D, 8-node element, was used under the condition of plane-strain behavior. To apply the boundary conditions of the mechanical model, the horizontal displacement of the nodes on the central line is considered zero; and to prevent rigid motion and solution convergence, the vertical displacement of one node with the minimum distance from the elements that are born during solution is considered zero. The mechanical solution continues as soon as the temperature of all elements reaches the ambient temperature.

7 RRSULTS

Fig. 7 shows the thermal history of some points of the upper surface of the model at the distances of 6, 20, and 40 *mm* from the central line within 1500 seconds. Corresponding to each pass, one temperature rise is seen in the thermal history of each point. The thermal solution results show that temperature gradient is more severe on the points close to the weld zone. The remarkable point in the figure is the low-temperature range of all the three welding passes in the *X*-groove joint as compared with the *V*-groove joint, which may affect the reduction of residual stresses and distortion.

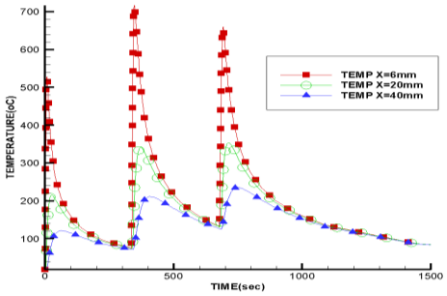

(a) *V*-groove joint

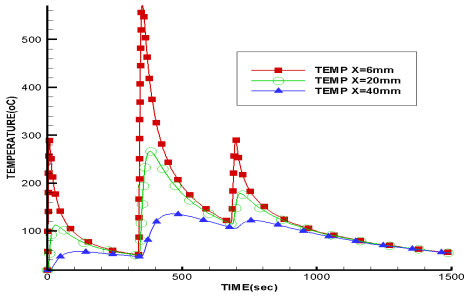

(b) *X*-groove joint

Fig.7
Thermal history of some points of the upper surface of model.

Fig. 8 shows temperature distribution for the periods after the start of each pass and before the start of the following pass. The figure proves that the heat has reached quickly along the thickness direction (Y direction) to the surface of the plate and from that moment on, heat transfer in the transverse direction (X direction) will have a greater contribution. Therefore, the role of conductive heat transfer is much more important than the one of convective heat transfer in the cooling weld. The effect is in a way that heat transfer will almost become one-directional approximately ten seconds after welding and this is seen better one hundred seconds after welding.

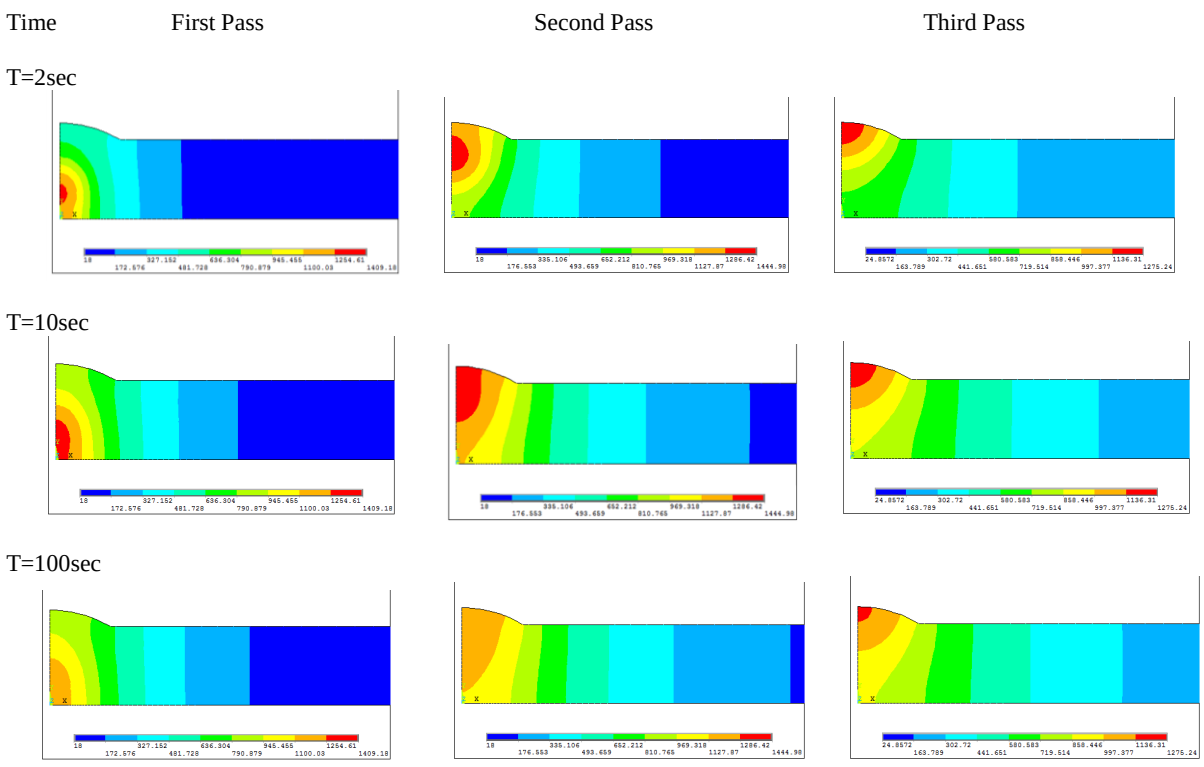

Fig.8
Temperature ($^{\circ}C$) distribution for periods after the start of each pass and before the start of the following pass in the V-groove joint.

The stresses parallel to weld line direction is called "longitudinal residual stresses" and the stresses perpendicular to weld line direction is called "transverse residual stresses". The distribution of longitudinal residual stresses and transverse residual stresses for the V-groove joint are shown in Figs. 9 and 10, respectively.

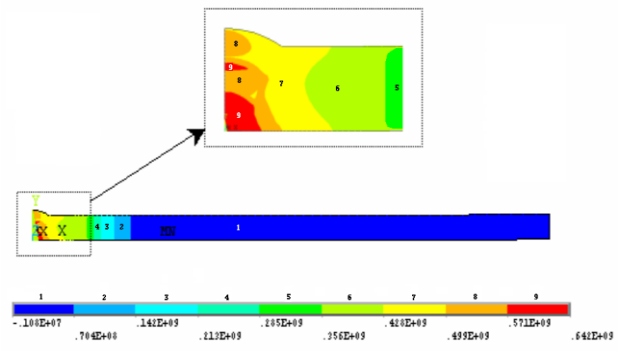

Fig.9
Distribution of longitudinal residual stresses (Pa) in the V-groove joint.

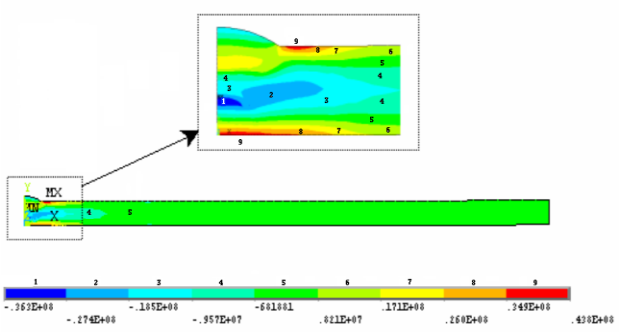

Fig.10
Distribution of transverse residual stresses (Pa) in the *V*-groove joint.

Fig. 11 compares the residual stresses for the upper surface of the model in the *V*-groove joint with the experimental results and the simulation proposed by Chang [7]. The figure shows an appropriate agreement between the research results and Chang's experimental and numerical results. Maximum transverse residual stresses occur near the weld zone. For longitudinal residual stresses, high tensile stresses are seen in the weld zone and the heat affected zone. The value of the longitudinal residual stresses is approximately bigger than the values presented by the experimental measuring method. The reason for this error should be found in assuming plane-strain behavior for the model and overlooking the Bauschinger effect. Generally, it is believed that the complex history of loading may play a crucial role in the different results of the finite element method and the experimental method.

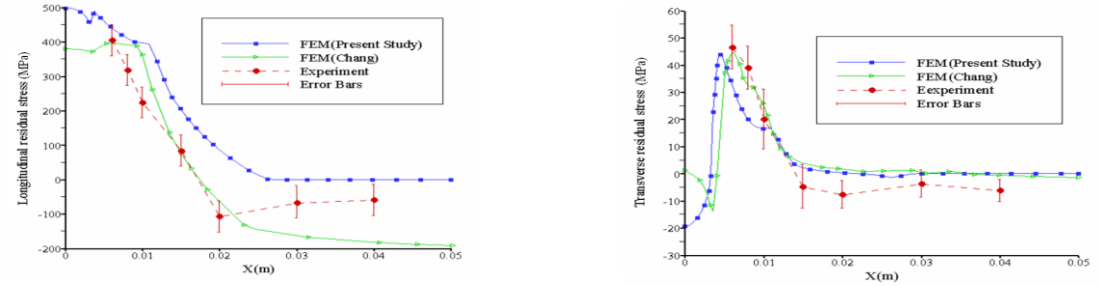

(a) Longitudinal residual stress (b) Transverse residual stress

Fig.11
Residual stresses versus normal distance to the weld line on the upper surface of model in the *V*-groove joint.

Fig. 12 shows von Mises residual stress distribution in *V*- and *X*-groove joints. The maximum residual stresses in the *V*- and *X*-groove joints are 677 *MPa* and 538 *MPa*, respectively. It shows that maximum von Mises residual stress was reduced by 20% by changing the joint geometry from *V*-groove to *X*-groove. Fig. 13 shows the numerical and experimental results of the distortion resulted from the welding process in terms of the distance from welding symmetry plane in both *V*- and *X*-groove joints. This research used a vertical digital altimeter for measuring the distortion of the upper surface of the plate. It shows that the numerical and experimental results are quite consistent. Fig.13 shows that maximum distortion reduced by 15% by changing the geometry from *V*-groove joint to *X*-groove joint. These conclusions are consistent with the experimental results of Vasantharaja et al [14].

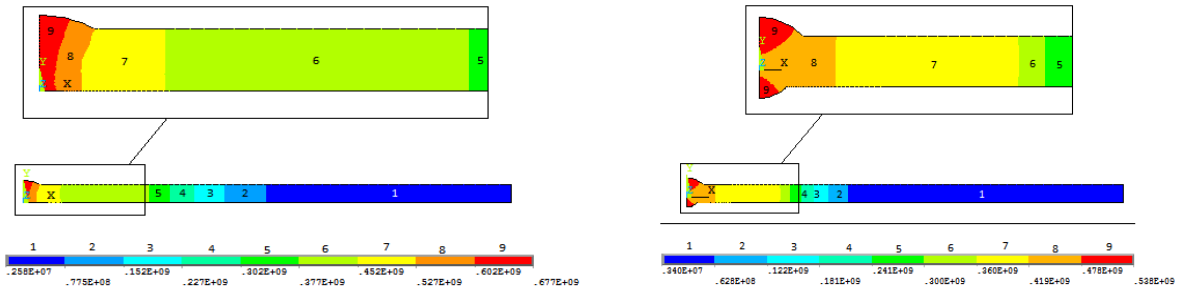

(a) V-groove joint (b) X-groove joint

Fig.12
Distribution of von Mises residual stresses (Pa).

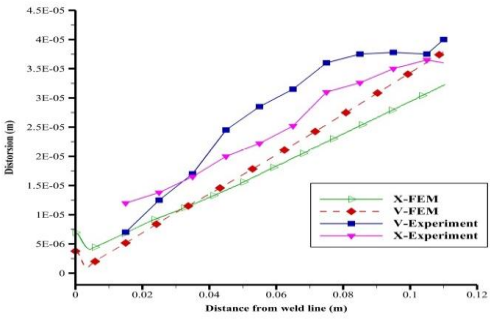

Fig.13
Distorsion versus normal distance to the weld line on the upper surface of model in the *X*- and *V*-groove joint.

8 CONCLUSION

- When the welding speed is much higher than the speed of heat conduction along the weld line, the model can be considered two-dimensional, which is effective and speeds up the simulation.
- Using the temperature calculated for each pass at the time of birth of the elements does not affect the results, but considerably increases the rate of convergence at the birth of the elements.
- Turbulence determines the contribution of surface and volumetric heat transfer in simulations. In this study, the total thermal power was simulated volumetrically, the accuracy of which indicates the high turbulence of the pool.
- Thermal solution results indicate that an increase in the temperature is found in the thermal history of every point corresponding to a pass and that the temperature gradient is steeper near the weld zone.
- After welding, heat has quickly reached the surface of the joint, propagated along the thickness (*Y* direction). Considering that convection is negligible on the surface compared to conduction, transverse heat transfer (*X* direction) plays a more important role from this moment on. The effect is in a way that heat transfer becomes almost one-directional after each weld pass.
- Longitudinal tensile residual stresses are high around the weld zone and this value becomes small by moving away from the weld zone.
- Maximum transverse residual stress is generated near a melting zone and this stress becomes almost zero on the points far from the zone.
- The results suggest that joint geometry is effective on residual stresses and distortion in the work piece. It was found that maximum von Mises residual stress and maximum distortion were reduced by 20 and 15%, respectively, when joint geometry was changed from *V*- to *X*-groove.

ACKNOWLEDGEMENTS

The authors are grateful for the assistance of the Islamic Azad University, Khomeinishahr Branch.

REFERENCES

[1] Rajabi H., Heidari A., 2018, Analysis and presenting an optimum post weld heat treatment cycle to maximum reduction of residual stresses of electron beam welding, *Journal of Mechanical Engineering and Vibration* **9**(2): 55-65.
[2] Zubairuddin M., Albert S. K., Vasudevan M., Mahadevan S., Chaudhari V., Suri V. K., 2017, Numerical simulation of multi-pass GTA welding of grade 91 steel, *Journal of Manufacturing Processes* **27**: 87-97.
[3] Forouzan M.R., Mirfalah Nasiri S.M., Mokhtari A., Heidari A., Golestaneh S.J., 2012, Residual stress prediction in submerged arc welded spiral pipes, *Materials & Design* **33**: 384-394.
[4] Portelette L., Roux J.-C., Robin V., Feulvarch E., 2017, A Gaussian surrogate model for residual stresses induced by orbital multi-pass TIG welding, *Computers & Structures* **183**: 27-37.
[5] Chaudhary S., Sahu S.A., Singhal A., 2018, On secular equation of SH waves propagating in pre-stressed and rotating piezo-composite structure with imperfect interface, *Journal of Intelligent Material Systems and Structures* **29**(10): 2223-2235.

[6] Cho S.H., Kim J.W., 2002, Analysis of residual stress in carbon steel weldment incorporating phase transformations, *Science and Technology of Welding and Joining* **7**(4): 212-216.
[7] Chang P.-H., Teng T.-L., 2004, Numerical and experimental investigations on the residual stresses of the butt-welded joints, *Computational Materials Science* **29**(4): 511-522.
[8] Yajiang L., Juan W., Maoai C., Xiaoqin S., 2004, Finite element analysis of residual stress in the welded zone of a high strength steel, *Bulletin of Materials Science* **27**(2): 127-132.
[9] Vasudevan M., 2007, *Computational and Experimental Studies on Arc Welded Austenitic Stainless Steel*, Ph.D. Thesis, Indian Institute of Technology, Madras, India.
[10] Palanichamy P., Vasudevan M., Jayakumar T., 2009, Measurement of residual stresses in austenitic stainless steel weld joints using ultrasonic technique, *Science and Technology of Welding and Joining* **14**(2): 166-171.
[11] Tseng K.-H., Hsu C.-Y., 2011, Performance of activated TIG process in austenitic stainless steel welds, *Journal of Materials Processing Technology* **211**(3): 503-512.
[12] Ganesh K.C., Vasudevan M., Balasubramanian K.R., Chandrasekhar N., Mahadevan S., Vasantharaja P., Jayakumar T., 2014, Modeling, prediction and validation of thermal cycles, residual stresses and distortion in Type 316 LN stainless steel weld joint made by TIG welding process, *Procedia Engineering* **86**: 767-774.
[13] Bhatti A.A., Barsoum Z., Murakawa H., Barsoum I., 2015, Influence of thermo-mechanical material properties of different steel grades on welding residual stresses and angular distortion, *Materials & Design* **65**: 878-889.
[14] Vasantharaja P., Vasudevan M., Palanichamy P., 2015, Effect of welding processes on the residual stress and distortion in type 316LN stainless steel weld joints, *Journal of Manufacturing Processes* **19**: 187-193.
[15] Varma Prasad V.M., Joy Varghese V.M., Suresh M.R., Siva Kumar D., 2016, 3D simulation of residual stress developed during TIG welding of stainless steel pipes, *Procedia Technology* **24**: 364-371.
[16] Bajpei T., Chelladurai H., and Ansari M. Z., 2016, Mitigation of residual stresses and distortions in thin aluminium alloy GMAW plates using different heat sink models, *Journal of Manufacturing Processes* **22**: 199-210.
[17] Sahu S.A., Singhal A., Chaudhary S., 2018, Surface wave propagation in functionally graded piezoelectric material: An analytical solution, *Journal of Intelligent Material Systems and Structures* **29**(3): 423-437.
[18] Wen S.W., Hilton P., Farrugia D.C. J., 2001, Finite element modelling of a submerged arc welding process, *Journal of Materials Processing Technology* **119**(1-3): 203-209.
[19] Golestaneh S.J., Ismail N., Ariffin M.K.A.M., Tang S.H., Forouzan M.R., Maghsoudi A.A., Firoozi Z., 2014, Minimization of residual stresses in submerged arc welding process of oil and gas steel pipes by committee machine, *Applied Mechanics and Materials* **564**: 519-524.
[20] Forouzan M.R., Heidari A., Golestaneh S.J., 2009, FE simulation of submerged arc welding of API 5L-X70 straight seam oil and gas pipes, *Journal of Computational Methods in Engineering* **28**(1): 93-110.
[21] Singh M.K., Sahu S.A., Singhal A., Chaudhary S., 2018, Approximation of surface wave velocity in smart composite structure using Wentzel–Kramers–Brillouin method, *Journal of Intelligent Material Systems and Structures* **29**(18): 3582-3597.
[22] Gery D., Long H., Maropoulos P., 2005, Effects of welding speed, energy input and heat source distribution on temperature variations in butt joint welding, *Journal of Materials Processing Technology* **167**(2-3): 393-401.
[23] Mazruei G., Heidari A., 2016, A new plan to connect aluminum tubes of subsurface structures, *Journal of Simulation and Analysis of Novel Technologies in Mechanical Engineering* **9**(3): 455-466.
[24] Da Nóbrega J., Diniz D., Silva A., Maciel T., de Albuquerque V., Tavares J., 2016, Numerical evaluation of temperature field and residual stresses in an API 5L X80 steel welded joint using the finite element method, *Metals* **6**(2): 28.
[25] Jia X., Xu J., Liu Z., Huang S., Fan Y., Sun Z., 2014, A new method to estimate heat source parameters in gas metal arc welding simulation process, *Fusion Engineering and Design* **89**(1): 40-48.
[26] Nasim K., Arif A.F.M., Al-Nassar Y.N., Anis M., 2015, Investigation of residual stress development in spiral welded pipe, *Journal of Materials Processing Technology* **215**: 225-238.
[27] Shen J., Chen Z., 2014, Welding simulation of fillet-welded joint using shell elements with section integration, *Journal of Materials Processing Technology* **214**(11): 2529-2536.